Materials Science & Engineering A 783 (2020) 139295

Contents lists available at ScienceDirect

Materials Science & Engineering A

journal homepage: www.elsevier.com/locate/msea

Influence of stress state on plastic flow and ductile fracture of three 6000-series aluminium alloys

Susanne Thomesen [a,*], Odd Sture Hopperstad [a,b], Ole Runar Myhr [a,c], Tore Børvik [a,b]

[a] Structural Impact Laboratory (SIMLab), Department of Structural Engineering, Norwegian University of Science and Technology (NTNU), NO 7491, Trondheim, Norway

[b] Centre for Advanced Structural Analysis (CASA), NTNU, NO 7491, Trondheim, Norway

[c] Hydro Aluminium, Research and Technology Development, NO 6601, Sunndalsøra, Norway

ARTICLE INFO

Keywords:
Aluminium alloys
Tension test
Triaxiality
Fractography

ABSTRACT

In this study, the plastic flow and ductile fracture of three 6000-series aluminium alloys commonly used for crash components in the automotive industry are characterised experimentally and the observations are related to microstructural features. The three alloys are used in the cast and homogenised condition after artificial ageing to temper T6 to ensure isotropic behaviour. Tension tests on smooth and notched axisymmetric specimens are carried out to reveal the stress–strain behaviour, ductility and fracture mechanisms of the materials for different stress states. Through the use of optical and scanning electron microscopes, the initial microstructure of the alloys and the fracture surfaces of the tension test specimens are investigated. The work-hardening of the alloys is analysed up to large strains. Whereas the ductility of two of the alloys falls into the trend of previous experimental data on 6000-series aluminium alloys, where the strain to failure decreases linearly with increasing yield stress, the third alloy stands out by combining high strength with high ductility. The excellent properties of the latter alloy are assumed to be due to a favourable size distribution of constituent particles.

1. Introduction

In the automotive industry, there is a constant need for enhancing product performance. Materials with high strength-to-weight ratio and good corrosion resistance that can easily be extruded are optimal for this purpose. For components subjected to impact conditions, such as bumper beams and crash boxes, the deformability and ability to absorb energy are vital characteristics. The combination of these characteristics is often found in 6000-series aluminium alloys, which explains the increasing use of aluminium in automotive safety components [1,2]. In such applications, energy absorption is a design criterion, and the yield strength, work-hardening and ductility of the alloy are important parameters. Crash components are subjected to large plastic deformations and should not fracture during the impact process as fracture marks the end of the energy absorption. By optimising the chemical composition and thermal processing of the alloy, it is possible to find materials that are well suited for this purpose.

In the design and modelling of aluminium components, it is important to understand the underlying microstructural mechanisms of the material at hand and how these affect the macroscopic response. As pure aluminium has low yield strength, the resistance has to be increased by some strengthening mechanisms. The addition of alloying elements is important as the strength increases with decreasing purity [3]. Alloying elements in solid solution, hardening precipitates and dispersoids affect the plastic flow by acting as pinning points for dislocations, thus contributing to an increased yield strength of the material as they increase the shear stress required to move the dislocations [4]. The non-shearable hardening precipitates and dispersoids will also contribute to an increased work-hardening as the dislocations pile up at these sites leading to high dislocation densities [5]. Zhao and Holmedal [6] found that a high density of non-shearable dispersoids will increase the initial work-hardening rate due to geometrically necessary dislocations that are generated around the dispersoids. At large plastic strains, the work-hardening rate is reduced when the density of geometrically necessary dislocations saturates. Solute elements will decrease the dynamic recovery rate of dislocations and thus contribute to a higher work-hardening rate [7,8].

It is well established that failure in ductile metals is dominated by nucleation, growth and coalescence of microscopic voids [9,10]. The voids nucleate at constituent particles or inclusions, either by decohesion between the matrix-particle interface [11] or by cracking of

* Corresponding author.
E-mail address: susanne.thomesen@ntnu.no (S. Thomesen).

https://doi.org/10.1016/j.msea.2020.139295
Received 24 October 2019; Received in revised form 17 March 2020; Accepted 23 March 2020
Available online 26 March 2020

the particle [4,8,12], or they may be created from coarse deformation bands or by intersecting slip planes [13]. Voids may also be present in the material before it is subjected to deformation [14]. The ductile failure process is highly affected by the stress state, defined by the stress triaxiality and the Lode parameter. Some of the first to address the effect of stress triaxiality was McClintock [15] and Rice and Tracy [16], and it has been widely investigated since that, see e.g. [17–25]. The Lode parameter, which characterises the deviatoric stress state, was not given noteworthy attention until rather recently in the study by Bao and Wierzbicki [26] on a 2000-series aluminium alloy, and has later been increasingly addressed in the literature, see e.g. [27–34].

The volume fraction and size distribution of constituent particles are assumed to be major factors determining the ductility of aluminium alloys, as these particles are typical sites for nucleation of voids and thus contribute in lowering the strain to failure [4]. The size of the constituent particles is important, as defects are most likely to be found in large particles, increasing the probability of particle cracking [35,36]. In addition to the constituent particles, the dispersoids, which are smaller particles introduced to control recrystallisation and grain growth, are assumed to influence the final stage of the ductile fracture process, i.e., during the void coalescence after the plastic flow has become localised [37]. The hardening precipitates, which are even smaller than the dispersoids, are assumed to only influence the ductile fracture process by the way they change the yield strength and work-hardening of the alloy [37]. Different alloying elements will influence the ductility in various ways, as Remøe et al. [38] showed in their investigations of four Al-Mg-Si alloys with different concentrations of some main alloying elements.

In this study, we are characterising the microstructure and the mechanical behaviour of three 6000-series aluminium alloys that are commonly used for crash components in the automotive industry. In previous works by two of the authors of this paper, with co-workers, see [4,8,39], four different aluminium alloys were investigated with respect to different alloying elements, microstructure, thermo-mechanical processing and artificial ageing procedures. These alloys ranged from low to intermediate strength. The main aim of the current study is to extend the previous research to 6000-series aluminium alloys with intermediate to high strength. To ensure isotropic behaviour, the alloys are used in the cast and homogenised condition, and they are artificially aged to temper T6. Tension tests on smooth and notched axisymmetric specimens are carried out to determine the stress–strain behaviour and to investigate the ductile fracture mechanisms of the materials. The initial microstructure and the fracture surfaces are investigated using optical and scanning electron microscopes. Based on the tensile tests on smooth specimens, the work-hardening of the alloys is analysed up to large strains. Two alloys exhibit the expected trend found in previous studies where the strain to failure decreases with increasing yield stress for alloys with similar microstructure. The third alloy displays an excellent combination of high strength and high ductility, most likely due to a favourable size distribution of the constituent particles, and deviates consequently from the expected trend.

2. Materials

Three 6000-series aluminium alloys are investigated in the current study. The materials were provided by Hydro Aluminium R&D Sunndal as DC-cast extrusion billets with a diameter of 95 mm. Table 1 provides the chemical composition of the three alloys. In the homogenisation heat treatment, the billets were heated to 575 °C with a heating rate of 200 °C/h, held at this temperature for 2 h and 15 min, and then cooled to room temperature with a cooling rate of 400 °C/h. This procedure corresponds to industrial practise.

Axisymmetric tensile specimens were made from the homogenised billets using a combination of spark erosion and turning. Subsequent to the machining, the specimens were solution heat-treated and artificially aged to temper T6, which is the peak strength condition. The applied procedure for the ageing heat treatment was as follows. The specimens were heated with a heating rate of 93 °C/min to 560 °C in a salt bath, solution heat-treated for 10 min after the temperature reached 555 °C, and then water quenched to room temperature. After 24 h storage at room temperature, the specimens were heated to 185 °C with a heating rate of 200 °C/h in an air circulating furnace, and kept at this temperature for 8 h after which they were water quenched to room temperature.

Table 1
Chemical compositions of the alloys in wt%.

Alloy	Mg	Si	Fe	Cu	Mn	Zn	Ti	Cr	Al
AA6061	0.903	0.621	0.209	0.204	0.038	0.054	0.106	0.060	Bal.
AA6063	0.470	0.512	0.206	0.001	0.047	0.003	0.006	0.001	Bal.
AA6110	0.828	0.720	0.196	0.203	0.506	0.003	0.026	0.157	Bal.

3. Experimental procedures

3.1. Microstructure characterisation

A sample was taken from each of the three materials in the cast and homogenised condition after being tempered to T6. The samples were cast in Epofix and further ground and polished down to 1 μm using SiC-paper and polishing pads, respectively. Then the samples were prepared for grain structure imaging through electropolishing in A2 (Struers electrolyte) at 30 V for 3 s and anodising at 20 V for 2 min. For all three alloys, the images were obtained using polarised light in a Reichert MeF3 A optical microscope with a 10 × objective.

The size and distribution of the constituent particles were obtained through image processing of backscattered electron micrographs. The images were taken using a Hitachi SU6600 Field Emission Scanning Electron Microscope (FESEM) operated at 10 kV. For this study, the anodised layer used in the grain structure investigations was removed by polishing the sample down to 1 μm.

The polished samples were further electropolished in A2 electrolyte at 30 V for 3 s to be used to perform a quantitative determination of the chemical composition of the α-phase constituent particles found in the three alloys. This was done using Energy Dispersive Spectroscopy (EDS) in a FEI Apreo SEM, operated at 15 kV.

The fracture surfaces of failed specimens were examined through secondary electron images obtained using a Zeiss Gemini SUPRA 55VP FESEM operated at 20 kV. All specimens were cleaned in an ultrasound bath using acetone before inserting them in the vacuum chamber of the FESEM.

3.2. Mechanical testing

Tensile tests were performed using smooth and notched axisymmetric specimens. The nominal geometry of the specimens is displayed in Fig. 1. Henceforth, the notched specimens with notch radius equal to 2.0 mm and 0.8 mm will be denoted R2.0 and R0.8, respectively. A combination of spark erosion and turning was used to machine the specimens from the cast and homogenised billets, aligning the tensile axis of the specimen with the longitudinal axis of the billet. The specimens were then heat treated to temper T6 as described in Section 2. It should be noted that due to problems during machining of the notched specimens, the actual diameter between the notch and the threaded ends was measured to 9.47 mm instead of the nominal value of 10 mm. The test series also included notched specimens with a notch radius of 0.2 mm [40]. However, difficulties in machining the narrow notch led to marked deviations in the notch radius, and these tests are therefore not reported here.

Three repeat tests of each specimen geometry were performed at room temperature for the three alloys under displacement-control in a Zwick Roell Z030 universal testing machine with a 30 kN load cell.

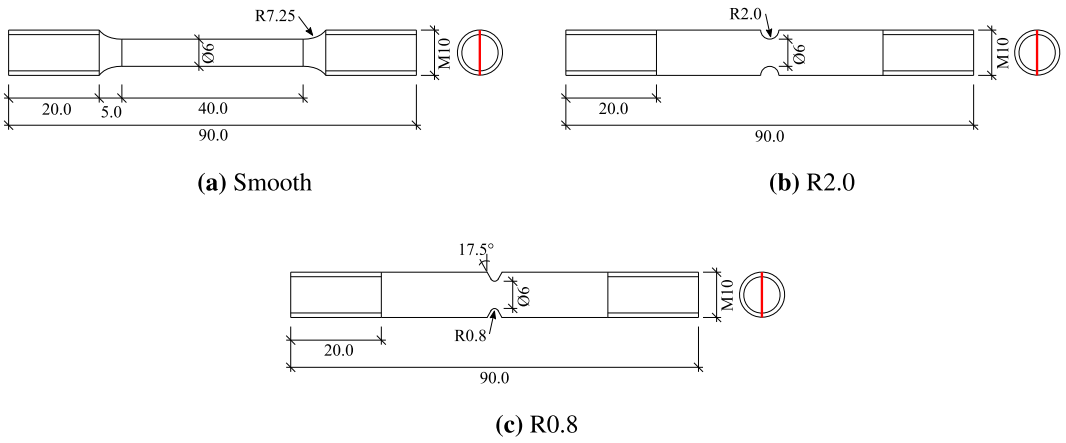

Fig. 1. Nominal geometries of the various tension test specimens. The red line in the rightmost figure in each sub-figure represents the radial direction of the billet, and was marked physically on the specimens. All measures are in mm. (For interpretation of the references to colour in this figure legend, the reader is referred to the web version of this article.)

In order to have quasi-static conditions, the crosshead velocity of the test machine was set equal to 1 mm/min for the smooth specimens and 0.15 mm/min for the notched specimens. Continuous measurements of the force and the diameter at the minimum cross section were provided all the way to failure [41]. The force F was measured directly from the load cell, while the diameter measurements were acquired using a high-speed, contact-less AEROEL XLS13XY laser gauge with 1 μm resolution. The laser gauge creates two perpendicular laser beams, each measuring 13 mm × 0.1 mm, that are pointed towards the detectors on the opposite side of the specimen. To assure that the minimum cross section was measured at all times, the laser gauge was installed on a mobile frame free to move vertically. The measured specimen diameters along the radial and circumferential directions of the billet are denoted D_1 and D_2, respectively.

As the specimens were initially axisymmetric, the current cross section was assumed to be elliptical. Thus, the initial and current cross-section area of the specimens could be obtained from the diameter measurements as

$$A_0 = \frac{\pi}{4} D_0^2 \quad \text{and} \quad A = \frac{\pi}{4} D_1 D_2 \tag{1}$$

Here, D_0 is the initial diameter of the specimen. Combined with the measured force, the true stress and the logarithmic strain could be calculated as

$$\sigma = \frac{F}{A} \quad \text{and} \quad \varepsilon = \ln\left(\frac{A_0}{A}\right) \tag{2}$$

where small elastic strains and plastic incompressibility were assumed in order to obtain the logarithmic strain. The plastic strain was then obtained through the relation $\varepsilon^p = \varepsilon - \sigma/E$, where E is the elastic modulus of the material. Note that the stress and strain measures in Eq. (2) represent average values over the minimum cross section of the smooth specimens after diffuse necking and for the notched specimens at all times.

4. Results and discussions

4.1. Initial microstructure

Fig. 2(a), (c) and (e) shows optical micrographs of the grain structures. A typical cast and homogenised grain structure, where the grains are equiaxed, is found for all three alloys. To determine the grain size of the alloys, the linear intercept method was applied, using the reticle inside the microscope. For the alloys AA6063 and AA6110, the grain size was measured over three lines of 100 grains each. The grains of alloy AA6061 were so large that it was not possible to count 100 grains over the length of the sample. Instead, a total of 263 grains were counted over four lines. Table 2 provides the measured average grain size for the three alloys.

Table 2
Grain size and constituent particle content.

Alloy	Average grain size [μm]	Area fraction of constituent particles [−]
AA6061	124	0.0050
AA6063	63	0.0061
AA6110	67	0.0076

To determine the particle size distribution, 30 images were taken over the surface of each sample. As evident from Fig. 2(b), (d) and (f), the constituent particles are mainly located at the grain boundaries. Fig. 3 presents the particle size distributions for the three alloys in terms of area fraction of constituent particles versus equivalent particle diameter $D_p = \sqrt{4A_p/\pi}$, where A_p is the area of the particle in the image plane. The obtained images were analysed using an in-house macro in the program ImageJ, and the obtained area fractions of constituent particles are given in Table 2. In these investigations, the different types of constituent particles that form during processing have not been distinguished. However, it is assumed that most of the constituent particles in the homogenised materials are α-phase constituent particles with composition $Al_{50}(Fe, Mn, Cr)_{12}Si_7$. Using EDS analyses, the chemical composition of 15 or more particles was obtained for each alloy, and the average atomic percentages (at%) found for the Si, Fe, Mn and Cr elements are given in Table 3. According to the composition of the α-phase constituent particles, the average atomic percentage of Si should be 7/12 = 58.3 at.%, but is found to be lower for all three alloys, possibly caused by noise from the surrounding material or inaccuracies in the measurements.

By inspection of the measurement details and the particle size distribution plots shown in Fig. 3, it is found that alloy AA6061 has the highest number of constituent particles, but also the largest fraction of small particles. Alloy AA6063 contains slightly larger particles than alloy AA6061, but they are significantly fewer in number. Alloy AA6110 has the highest area fraction of the three alloys, cf. Table 2. In addition, this alloy contains the highest concentration of large particles among the three alloys, which also is evident from the micrographs in Fig. 2(b), (d) and (f).

4.2. Stress–strain behaviour

From the measurements of the current diameters all the way to fracture, the stress–strain curves in terms of the true stress and the logarithmic strain were calculated, as described in Section 3.2. The

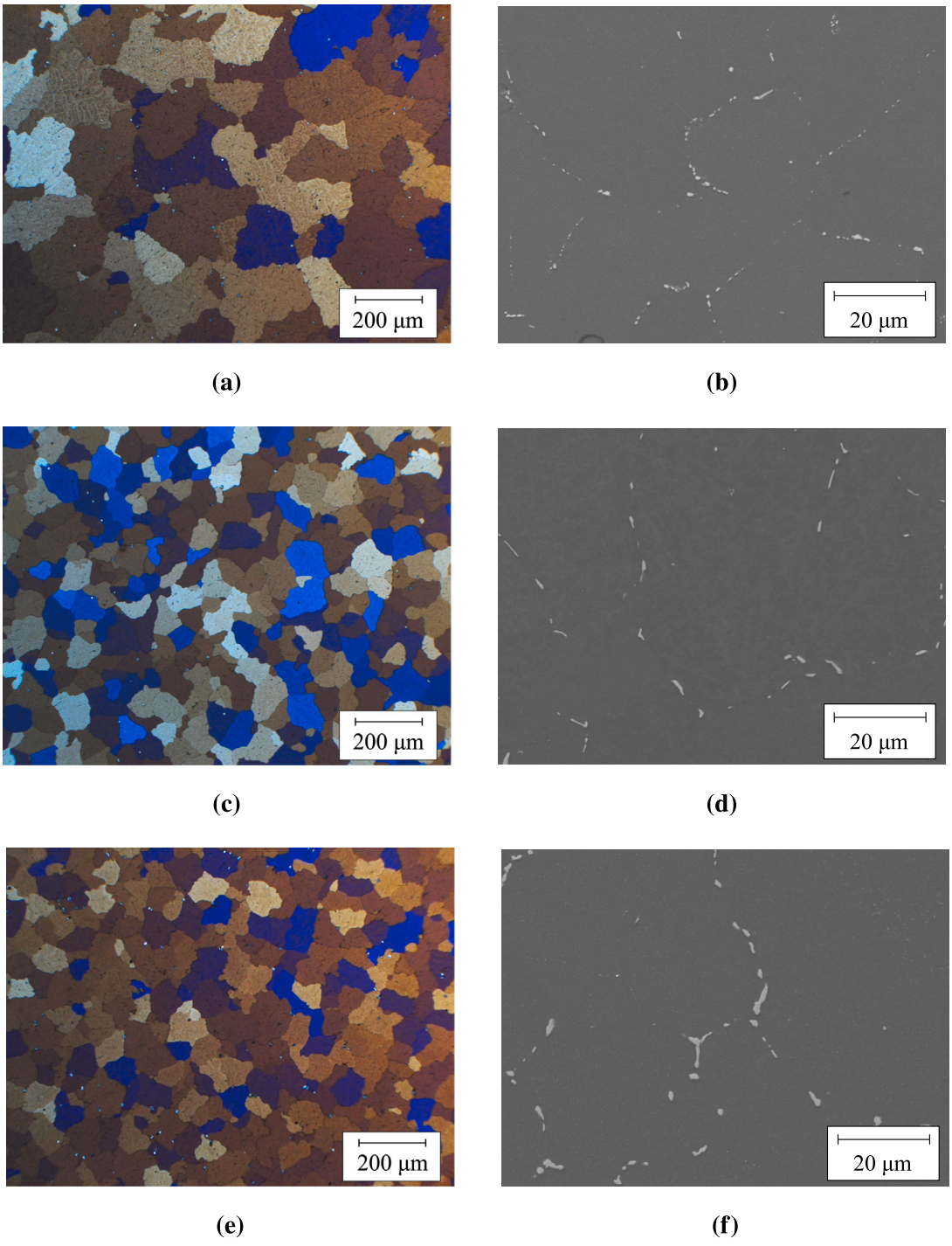

Fig. 2. Grain structure of (a) AA6061, (c) AA6063 and (e) AA6110, and distribution of constituent particles in (b) AA6061, (d) AA6063 and (f) AA6110.

Table 3
Quantitative characterisation of the α-phase constituent particles, $Al_{50}(Fe,Mn,Cr)_{12}Si_7$.

Alloy	Si/(Fe+Mn+Cr) [at%]	Fe/(Fe+Mn+Cr) [at%]	Mn/(Fe+Mn+Cr) [at%]	Cr/(Fe+Mn+Cr) [at%]
AA6061	50.6	92.1	5.9	2.1
AA6063	49.6	91.3	8.6	0.1
AA6110	56.1	49.8	43.4	6.8

resulting stress–strain curves are shown in Fig. 4. The effect of specimen geometry for each alloy is illustrated in Fig. 4(a)–(c), where a representative stress–strain curve is selected from the three repeat tests. The stress–strain behaviour of the three alloys is compared in Fig. 4(d), where the stress–strain curves from all repeat tests on the smooth specimens are presented. The scatter in the stress level between the repeat tests was negligible. In all subfigures of Fig. 4, the black crosses (×) mark the point of failure in the experiments. The failure strain, defined as the logarithmic strain at maximum true stress, was obtained in the three repeat tests for all combinations of alloy and specimen geometry, and is presented in Table 4. In contrast to the flow stress, the scatter in the failure strain between repeat tests is significant, which is also clearly seen for the tests on the smooth specimens in Fig. 4(d).

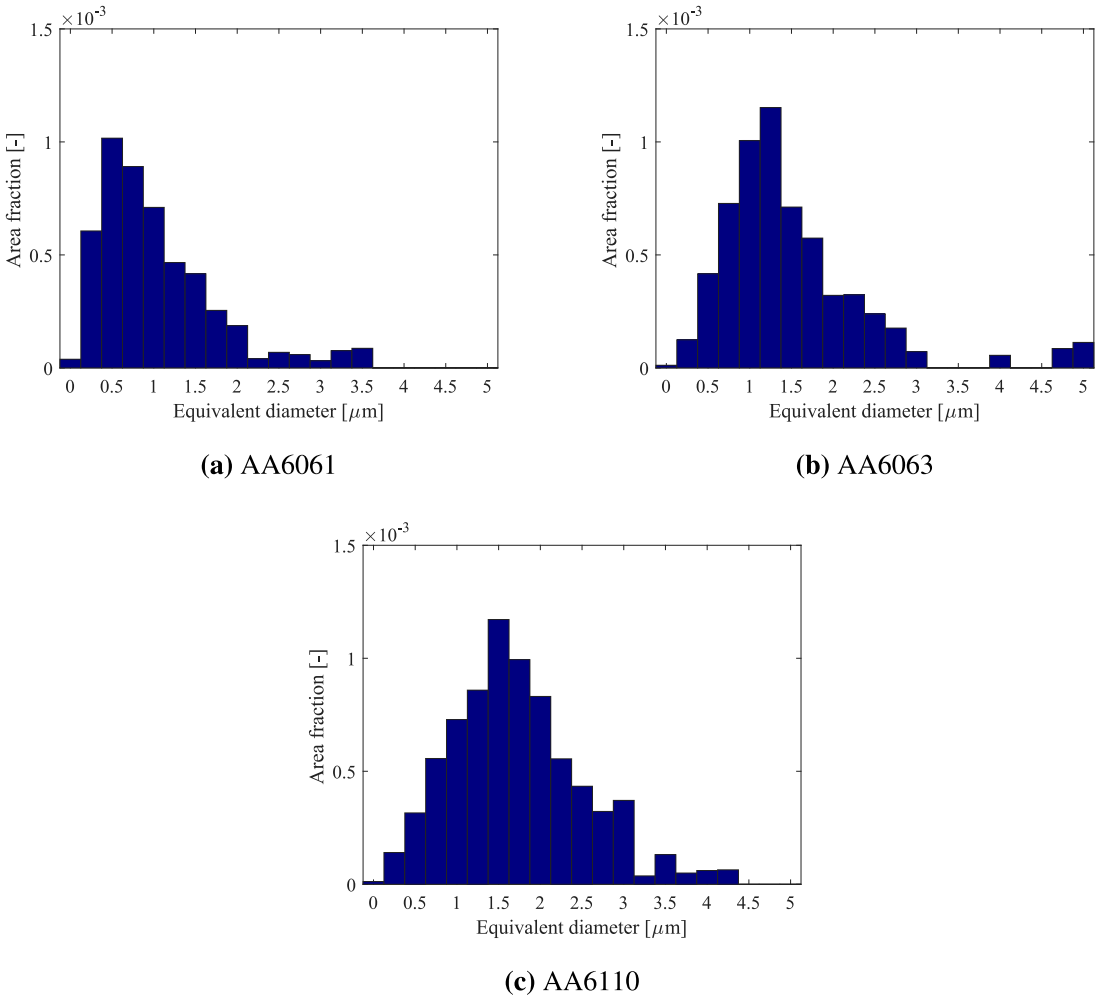

Fig. 3. Particle size distributions for the three alloys in terms of area fraction of constituent particles versus equivalent diameter.

Table 4
Failure strain from all repeat tests.

Alloy	Smooth	R2.0	R0.8
AA6061	0.5050	0.1343	0.1644
	0.5236	0.1505	0.1894
	0.5854	0.1462	0.1997
AA6063	0.5105	0.1483	0.2095
	0.5505	0.1442	0.2108
	0.5268	0.1349	0.2039
AA6110	0.2961	0.0883	0.0912
	0.3554	0.0861	0.0889
	0.3571	0.0744	0.0915

The notch strengthening effect is illustrated for all alloys in Fig. 4(a)–(c). It is normally anticipated that an increase in stress triaxiality, as obtained by a sharper notch, will lead to an increase in the stress level and a decrease of the ductility. The relation between the R2.0 and R0.8 specimens clearly deviates from this presumed pattern as the R2.0 specimens have lower failure strain than the R0.8 specimens. Although the results are not quite as expected, similar observations have been made previously, see e.g. [22,25]. This observation was also investigated using finite element simulations in Thomesen [40]. From the simulations, it was clear that fracture initiated in the centre of the minimum cross section of the R2.0 specimen, while for the R0.8 specimen fracture initiated close to the notch root. The stress triaxiality versus equivalent plastic strain curves of the two specimens deviated markedly, and the corresponding differences in failure modes were assumed to be the main reason for the unexpected pattern in failure strain found in the tension tests of the notched specimens.

4.3. Work-hardening

As the stress and strain fields are inhomogeneous at all strains in the notched specimens and after diffuse necking in the smooth specimens, it is not possible to obtain information about the work-hardening of the materials up to fracture directly from the tensile tests. This information is given in terms of equivalent stress–strain curves, which usually is obtained using finite element simulations through inverse modelling. However, by correcting the experimental true stress versus logarithmic strain curves using the approach suggested by Bridgman [42], a good estimate of the equivalent stress–strain curves can be obtained. The approach applied in this study is described in the following.

The flow stress is given by

$$\sigma_f = \sigma_0 + R(p), \quad R(p) = \sum_{i=1}^{3} R_i(p) \tag{3}$$

where

$$R_i(p) = Q_i(1 - \exp(-C_i p)) \tag{4}$$

In these equations, p is the equivalent plastic strain, σ_0 is the initial yield stress, and Q_i and C_i are hardening constants. The equivalent plastic strain p was set equal to the plastic strain ε^p calculated based on the measured diameters. The hardening variable R has three terms assumed to represent the elastic–plastic transition (R_1), stage III hardening (R_2)

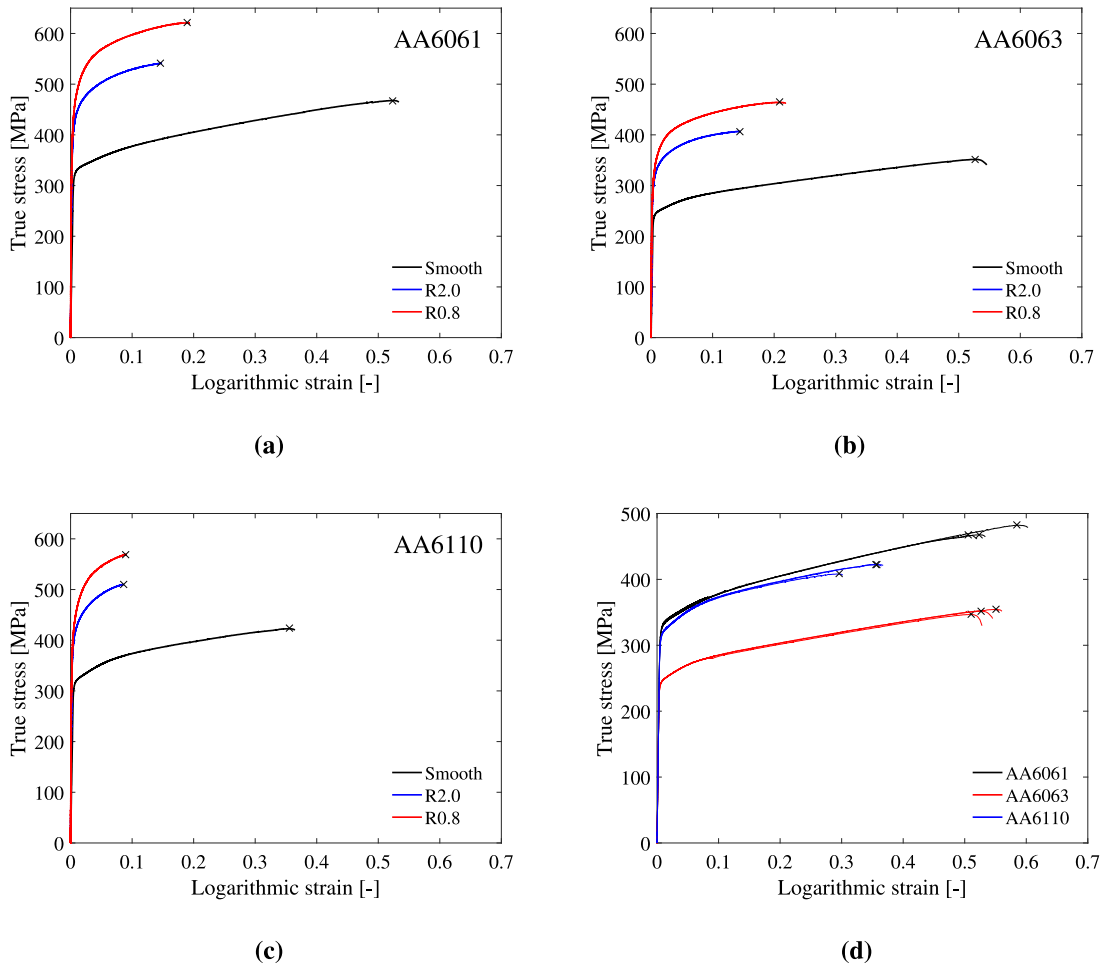

Fig. 4. Representative stress–strain curves for all specimen geometries of alloy (a) AA6061, (b) AA6063 and (c) AA6110, and (d) all repeat tests of the smooth specimen of the three alloys. The × marks failure at maximum true stress.

and stage IV hardening (R_3). Using Eqs. (3) and (4), the hardening rate θ of the material can be calculated as

$$\theta(p) = \frac{\mathrm{d}\sigma_f}{\mathrm{d}p} = \sum_{i=1}^{3} C_i Q_i \exp(-C_i p) \tag{5}$$

The yield stress σ_0 and the hardening parameters Q_i and C_i were determined based on a curve fit of the flow stress to the Bridgman-corrected experimental stress–strain curves by means of the method of least squares. The Bridgman-corrected flow stress after diffuse necking in the smooth specimens was estimated by [42]

$$\sigma_f = \frac{\sigma}{(1 + (2R_c/a))[\ln(1 + (a/2R_c))]} \tag{6}$$

where R_c is the radius of curvature of the neck and a is the specimen radius at the neck. The Bridgman equation was combined with an empirical expression for the ratio a/R_c suggested by LeRoy et al. [43]

$$a/R_c = 1.1(p - p_u), \qquad p > p_u \tag{7}$$

where p_u is the equivalent plastic strain at necking. Parameter sets based on the Bridgman–LeRoy correction are compiled in Table 5. These parameters were used in finite element simulations of the tensile tests on the smooth specimens in Thomesen [40] and excellent agreement was found. Accordingly, the parameter sets in Table 5 were deemed accurate and adopted in the analysis of the work-hardening of the alloys in this study.

The flow stress σ_f and the hardening rate θ are plotted against the equivalent plastic strain p in Fig. 5(a). The curves are plotted to the equivalent plastic strain corresponding to failure in the experiments.

Table 5
Yield stress and hardening parameters.

Alloy	σ_0 [MPa]	C_1 [–]	Q_1 [MPa]	C_2 [–]	Q_2 [MPa]	C_3 [–]	Q_3 [MPa]
AA6061	288.2	891.3	37.4	19.9	40.5	1.85	92.4
AA6063	220.1	1075.3	20.5	28.0	35.1	0.93	105.4
AA6110	277.7	1311.7	35.9	19.1	63.6	0.01	6888.4

The flow stress curves of the AA6061 and AA6110 alloys are similar, but the hardening rate differs significantly. The hardening rate of alloy AA6110 is higher initially, but it saturates more rapidly, and for large strains alloy AA6061 has the highest hardening rate. The AA6063 alloy has a markedly lower flow stress level and the hardening rate is consistently lower than for the AA6061 alloy up to failure.

Fig. 5(b) presents Kocks–Mecking plots for the three alloys in which the hardening rate θ is plotted against the hardening R, which represents the dislocation strengthening of the material. The curves are plotted to an equivalent plastic strain of 1, where the × marks the point of failure in the experiments. The high hardening rate of the AA6110 alloy in stage III (i.e., subsequent to the elastic–plastic transition) with its rapid saturation into stage IV hardening and the relatively low hardening rate of the AA6063 alloy are more clearly visualised in this plot. The AA6061 alloy exhibits the most hardening of the three alloys at failure and the highest hardening rate for large strains (stage IV).

As seen, the yield stress of the AA6061 and AA6110 alloys is similar and significantly higher than the yield stress of the leaner AA6063 alloy. To explain the differences in strength, calculations with the

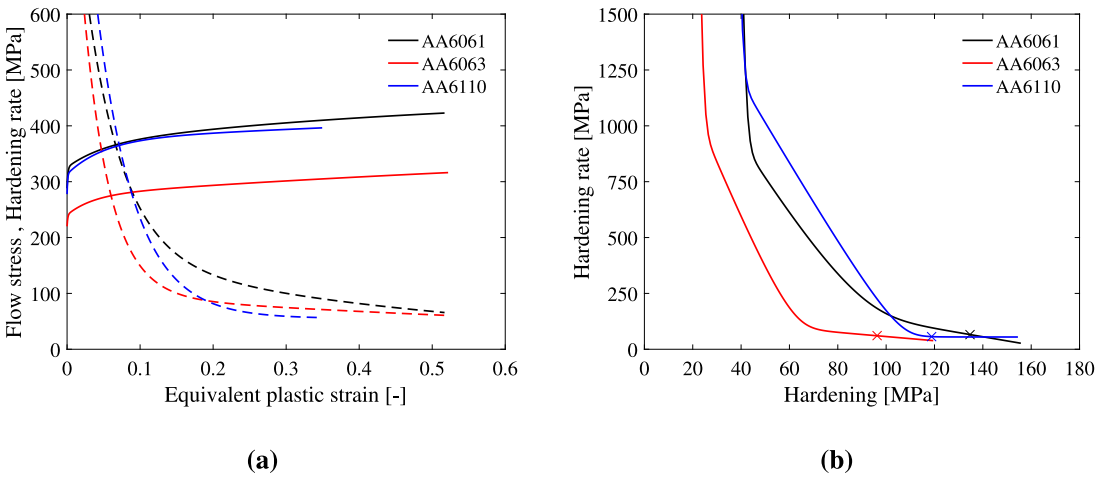

Fig. 5. (a) Flow stress σ_f (solid line) and hardening rate θ (dashed line) versus the equivalent plastic strain p to failure for the three alloys, and (b) hardening rate θ versus hardening R up to an equivalent plastic strain of 1, where the × marks failure in the experiments.

nanostructure model NaMo [44] were conducted based on the chemical compositions of the alloys and the thermal treatment, see Thomesen [40] for details. These calculations indicate that the reason for the lower yield stress of the AA6063 alloy is partly a lower solute content and partly a lower volume fraction of hardening precipitates. According to the NaMo calculations, alloy AA6063 has the lowest solute content of the three alloys in terms of Mg and Si in solid solution. For alloys AA6110 and AA6061, the calculated solid solution concentrations of Mg and Si after homogenisation are similar, with slightly higher Si and lower Mg concentrations for the former alloy. There is, however, a significant difference in the solid solution concentration of Mn between the two alloys, since AA6110 contains a substantial amount of Mn, while the Mn level is low for AA6061. Even though some of the Mn will be tied up in constituent particles and dispersoids that form during casting and homogenisation, some will remain in solid solution after the final ageing heat treatment. As the solute content determines the rate of dynamic recovery, this should imply that the stage III hardening rate is highest for AA6110, intermediate for AA6061, and lowest for AA6063, which agrees with the experimental findings.

When evaluating the work-hardening in stage IV, i.e., for large plastic strains after diffuse necking, it should be kept in mind that there is a contribution from texture evolution that cannot be separated from the contribution from dislocation strengthening without performing crystal plasticity simulations. Such simulations were conducted by Khadyko et al. [45] and the results indicate that the Taylor factor in uniaxial tension of an aluminium alloy with random texture increases significantly with plastic straining. Thus, the contribution from texture evolution may be significant and should be kept in mind.

4.4. Tensile ductility

A linear relation between the yield stress and the failure strain of different aluminium alloys with a constant or similar microstructure is often observed, where the ductility decreases with increasing yield strength, see e.g. [8,46,47]. In Fig. 4(d), the three repeat tests of the smooth specimens are compared for the three alloys. Alloy AA6061 clearly deviates from this pattern, but in a positive manner. This alloy has a slightly higher strength level than the AA6110 alloy and a significantly higher strength than the AA6063 alloy. Despite this, alloys AA6061 and AA6063 have similar ductility, which is quite remarkable, especially when considering the larger grain size of the AA6061 alloy (see Table 2). This finding is better illustrated in Fig. 6 where the failure strain from the tensile tests on smooth specimens is plotted against the yield stress, defined as the true stress at 0.2% plastic strain. In Fig. 6(a), the three alloys of this study are shown together with the cast and homogenised Al-0.5Mg-0.4Si alloy in temper T6 from Westermann et al. [39]. It is evident that the failure strain decreases linearly with the yield stress for the AA6110, AA6063 and Al-0.5Mg-0.4Si alloys. Note that the dashed line in the figure is not fitted to the experimental data but represents the observed trend. In contrast, the failure strain of the AA6061 alloy is located significantly above the trendline for the other alloys. The failure strains of these four materials are also shown in Fig. 6(b) together with those of the Al-0.5Mg-0.4Si alloy in tempers T6x (underaged) and T7 (overaged) from Westermann et al. [39], and the cast and homogenised Al-0.2Fe, Al-0.8Fe, Al-1.2Mn and Al-0.5Mg-0.4Si alloys from Westermann et al. [8] that were stored at room temperature after homogenisation. Two dashed lines are drawn here to illustrate the trends observed for the two data sets, where the rightmost trendline is the same as in Fig. 6(a). The main trend for both data sets is that the failure strain decreases linearly with increasing yield stress, but the slope of the two trendlines differs markedly due to the different microstructures of the alloys. The failure strains of the Al-0.5Mg-0.4Si alloy in tempers T6x and T7 fit well to the trendline drawn for the AA6110, AA6063 and Al-0.5Mg-0.4Si alloys in temper T6, whereas the AA6061 alloy in temper T6 still stands out with its combination of high yield strength and high tensile ductility.

The influence of the notch geometry on the failure strain, or the notch sensitivity, is illustrated in Fig. 7, where the normalised failure strain of an alloy is defined as the failure strain of a notched specimen (R2.0 or R0.8) divided by the failure strain of the smooth specimen. Here, the values for the plot are obtained using the average values for all repeat tests. It is seen that the notch sensitivity is somewhat similar for the R2.0 specimen of all alloys. For the R0.8 specimen, however, the notch sensitivity is significantly stronger for the high strength AA6110 alloy than for the intermediate strength AA6063 alloy, which is as expected. In contrast, the R0.8 specimen of the AA6061 alloy exhibits only slightly more notch sensitivity than the AA6063 alloy despite the large difference in yield strength. Put differently, the loss of ductility due to the higher stress triaxiality induced by the notch of the R0.8 specimen is more significant for the AA6110 alloy than for the AA6061 alloy, even though these two alloys have similar yield strengths.

4.5. Fracture surfaces

The fracture surfaces of the tested specimens were imaged to investigate the fracture mechanisms of the different alloys and specimen geometries. Fig. 8(a)–(c) show macroscopic images of the fractured surfaces of the smooth specimens for the three alloys. No significant difference in appearance of the fracture surfaces is observed between the alloys, and a typical cup-and-cone fracture is found as the main

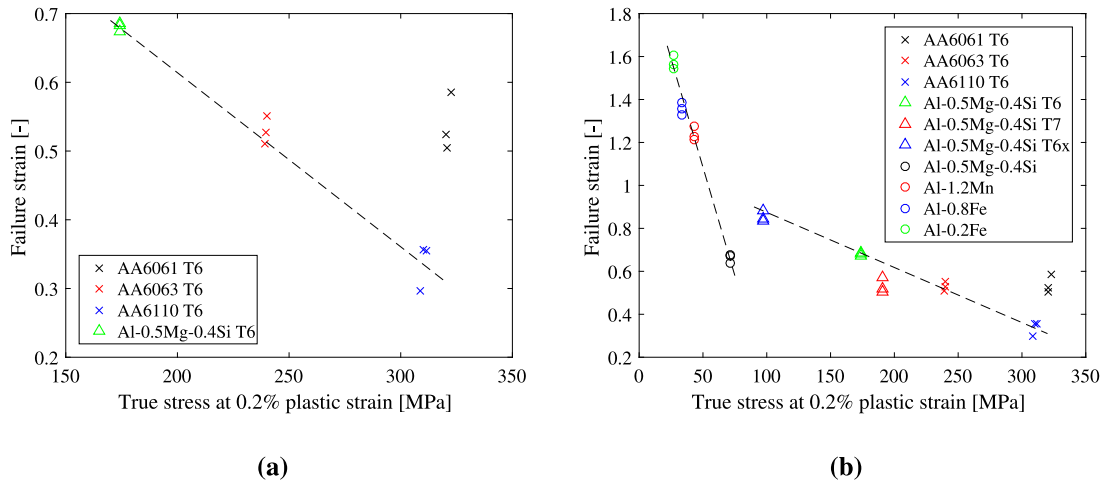

Fig. 6. Failure strain versus true stress at 0.2% plastic strain for the three alloys of this study together with data from Westermann et al. [8,39]. All experimental data are from tensile tests on smooth specimens of the same geometry. Note that the dashed lines are not fitted to the experimental data, but added to illustrate trends.

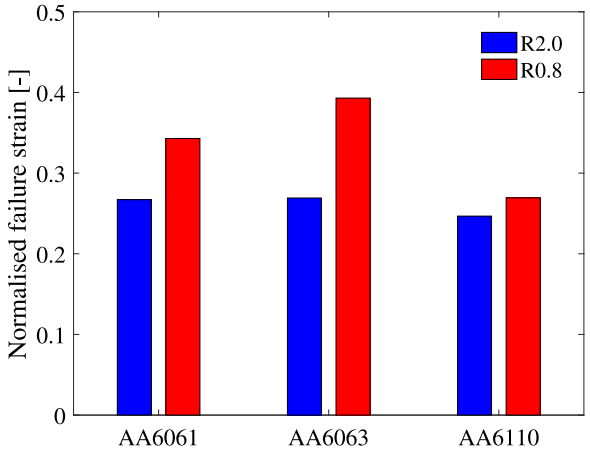

Fig. 7. Notch sensitivity for the alloys in terms of normalised failure strain as function of specimen type. The normalised failure strain of an alloy is defined as the failure strain of the notched specimen (R2.0 or R0.8) divided by the failure strain of the smooth specimen. Average values for all repeat tests are used to obtain the values for this plot.

global fracture mode. This indicates that the fracture initiates in the centre of the smooth specimens and grows outwards. Global images of the fracture surfaces of the notched specimens were obtained as well, but are not shown as the main observations found for the smooth specimens are also valid for these geometries. It can be seen from the images of the smooth specimens that the cross-sectional area at fracture is larger for the AA6110 alloy than the other two. From Fig. 4(d) it was seen that the AA6110 alloy had significantly lower failure strain than the AA6061 and AA6063 alloys, which corresponds well with the macroscopic images.

Images of the central part of the fractured specimens were taken with higher magnification. These images are shown in Fig. 8(d)–(f) for the smooth specimens, in Fig. 8(g)–(i) for the R2.0 specimens and in Fig. 8(j)–(l) for the R0.8 specimens. A classic dimpled surface is seen in all images, which is an indicator of ductile fracture. As commonly observed (see e.g. [8]), the fracture surface consists of two categories of dimples; mainly a lower density of large dimples, combined with small areas covered with a high density of small dimples. By comparing the fracture surfaces of the smooth and notched specimens it is observed that the dimples appear more shallow in the case of the notched specimens. This is caused by the higher stress triaxiality of the notched specimens, and indicates less ductile behaviour, which is also observed from the stress–strain curves in Fig. 4. In addition, the dimples of the notched specimens seem to have larger diameter compared to the smooth specimens, which again is linked to the higher stress triaxiality.

Constituent particles are seen at the bottom of the dimples in all three alloys. Some dimples do not contain any particles, but this does not exclude that they have been present as they may have fallen out or still be present in the opposite fracture surface. The particles are assumed to be nucleation sites for voids due to particle cracking and/or decohesion between the particles and the matrix. The large amount of particles observed shows that void initiation, growth and coalescence are the main physical mechanisms of fracture in these alloys. Especially in alloy AA6110 a large amount of constituent particles, and what appears to be small dispersoids, can be observed. From the particle characterisation in Fig. 3, a significantly higher area fraction of particles was found for this alloy compared to the AA6061 and AA6063 alloys. As already mentioned, the AA6110 alloy has the lowest failure strain and the highest particle density of the three alloys.

Based on the fractography, the fracture mechanisms are found to be similar in the three alloys and consist of nucleation, growth and coalescence of voids around the iron-rich constituent particles. The AA6063 and AA6110 alloys exhibit failure strains that are consistent with those found for an artificially aged Al-0.5Mg-0.4Si alloy by Westermann et al. [39], in the sense that the tensile ductility decreases linearly with increasing yield stress for these materials. The physical mechanism behind this trend is assumed to be an increased rate of void nucleation due to the higher stress level and thus a decrease of the ductility (e.g. [35]). In contrast, the AA6061 alloy has about the same failure strain as the AA6063 alloy whereas the yield strength is approximately 33% higher. The AA6110 alloy has similar yield stress as the AA6061 alloy, but approximately 38% lower failure strain. Furthermore, the notch sensitivity (or loss of ductility due to a notch) is similar for the AA6061 and AA6063 alloys, but more pronounced for the AA6110 alloy. The main reason for these differences in ductility is believed caused by differences in the volume fraction and size distribution of the constituent particles. Based on the area measurements, the constituent particle fraction is markedly lower in the AA6061 and AA6063 alloys than in the AA6110 alloy, and, in addition, the average size of the constituent particles is markedly smaller in the AA6061 alloy than in the other two. According to the study of Hannard et al. [35], the size distribution of the constituent particles as well as their spatial distribution are key elements determining the tensile ductility of 6000-series aluminium alloys. It is also interesting to note that the high ductility of the AA6061 alloy is achieved with a grain size that is about twice as large as in the other two alloys. A large grain size is expected to be negative for the ductility [48], but for the AA6061 alloy the effect of the large grains seems to be more than compensated for by the small-sized constituent particles.

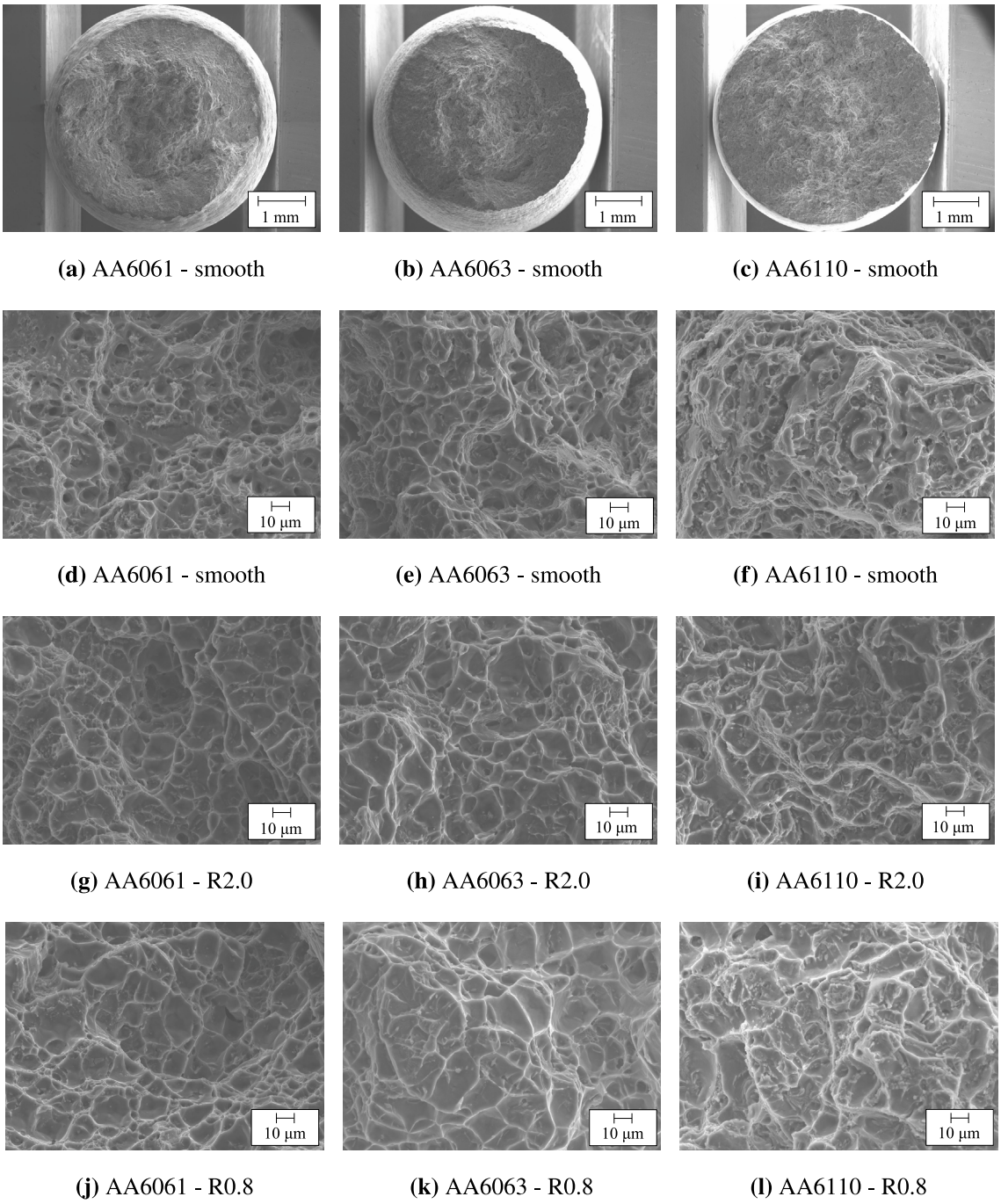

Fig. 8. Fracture surfaces: (a)–(c) global images of the smooth specimens, and local images from the central part of (d)–(f) the smooth specimens, (g)–(i) the R2.0 specimens and (j)–(l) the R0.8 specimens.

5. Concluding remarks

The plastic flow and ductile fracture of three 6000-series aluminium alloys, i.e., AA6061, AA6063 and AA6110, were investigated experimentally by tensile testing of smooth and notched axisymmetric specimens. The cast and homogenised alloys were tested in the T6 temper, which is the peak strength condition.

The main findings are summarised as follows:

- The main mechanism for fracture was found to be nucleation, growth and coalescence of voids, which was evident from the dimple structure observed in the images of the fracture surfaces.
- Alloy AA6110 has the highest work-hardening rate in stage III, followed by alloy AA6061 and AA6063, respectively. However, the hardening rate of alloy AA6110 saturates rapidly into stage IV, where alloy AA6061 experiences the most hardening and the highest hardening rate among the alloys. Differences in solute content of the alloys were assumed to cause the observed variations in stage III hardening due to its influence on the dynamic recovery rate.
- The general trend for cast and homogenised aluminium alloys is that the tensile ductility decreases linearly with increasing yield stress for similar microstructure. The slope of the trendline depends critically on the microstructural features of the alloys.

- An exception to this trend is the high-strength AA6061 alloy, which has similar ductility as the intermediate-strength AA6063 alloy and markedly higher ductility than the high-strength AA6110 alloy. The main reason for the high ductility of AA6061 is assumed to be the smaller sized constituent particles.

This study has extended previous research on the stress–strain behaviour of 6000-series aluminium alloys, and has laid the foundation for future development of microstructure-based constitutive models of plasticity and fracture for this class of materials. In a forthcoming study, the plastic flow and fracture of the same alloys are investigated experimentally after extrusion and artificial ageing, where the effects of plastic, morphological and topological anisotropy are highlighted.

Data availability

The raw/processed data required to reproduce these findings cannot be shared at this time as the data also forms part of an ongoing study. However, the data used to support the findings of this study may be made available from the corresponding author upon request.

Declaration of competing interest

The authors declare that they have no known competing financial interests or personal relationships that could have appeared to influence the work reported in this paper.

CRediT authorship contribution statement

Susanne Thomesen: Formal analysis, Investigation, Writing - original draft, Writing - review & editing, Visualization. **Odd Sture Hopperstad:** Conceptualization, Writing - original draft, Writing - review & editing, Supervision. **Ole Runar Myhr:** Formal analysis, Writing - review & editing. **Tore Børvik:** Conceptualization, Writing - review & editing, Supervision.

Acknowledgements

The authors gratefully appreciate the financial support from Norwegian University of Science and Technology (NTNU) and the Research Council of Norway through the FRINATEK Program FractAl, Project No. 250553.

References

[1] W.S. Miller, L. Zhuang, J. Bottema, A.J. Wittebrood, P. De Smet, A. Haszler, A. Vieregge, Recent development in aluminium alloys for the automotive industry, Mater. Sci. Eng. A 280 (1) (2000) 37–49.
[2] H. Zhong, P.A. Rometsch, L. Cao, Y. Estrin, The influence of Mg/Si ratio and Cu content on the stretch formability of 6xxx aluminium alloys, Mater. Sci. Eng. A 651 (2016) 688–697.
[3] Q. Zhao, M. Slagsvold, B. Holmedal, Comparison of the influence of Si and Fe in 99.999% purity aluminum and in commercial-purity aluminum, Scr. Mater. 67 (2) (2012) 217–220.
[4] K.O. Pedersen, I. Westermann, T. Furu, T. Børvik, O.S. Hopperstad, Influence of microstructure on work-hardening and ductile fracture of aluminium alloys, Mater. Des. 70 (2015) 31–44.
[5] J.D. Embury, W.J. Poole, D.J. Lloyd, The work hardening of single phase and multi-phase aluminum alloys, in: Aluminium Alloys 2006 - ICAA10, in: Materials Science Forum, vol. 519–521, Trans Tech Publications, 2006, pp. 71–78.
[6] Q. Zhao, B. Holmedal, Modelling work hardening of aluminium alloys containing dispersoids, Phil. Mag. 93 (23) (2013) 3142–3153.
[7] Ø. Ryen, O. Nijs, E. Sjölander, B. Holmedal, H.-E. Ekström, E. Nes, Strengthening mechanisms in solid solution aluminum alloys, Metall. Mater. Trans. A 37 (6) (2006) 1999–2006.
[8] I. Westermann, K.O. Pedersen, T. Furu, T. Børvik, O.S. Hopperstad, Effects of particles and solutes on strength, work-hardening and ductile fracture of aluminium alloys, Mech. Mater. 79 (2014) 58–72.
[9] T.L. Anderson, Fracture Mechanics: Fundamentals and Applications, third ed., CRC Press, Taylor & Francis Group, 2005.
[10] A.A. Benzerga, J.-B. Leblond, Ductile fracture by void growth to coalescence, in: Advances in Applied Mechanics, vol. 44, Elsevier, 2010, pp. 169–305.
[11] A. Pineau, A.A. Benzerga, T. Pardoen, Failure of metals I: Brittle and ductile fracture, Acta Mater. 107 (2016) 424–483.
[12] E. Maire, S. Zhou, J. Adrien, M. Dimichiel, Damage quantification in aluminium alloys using in situ tensile tests in X-ray tomography, Eng. Fract. Mech. 78 (15) (2011) 2679–2690.
[13] K.O. Pedersen, H.J. Roven, O.-G. Lademo, O.S. Hopperstad, Strength and ductility of aluminium alloy AA7030, Mater. Sci. Eng. A 473 (1–2) (2008) 81–89.
[14] H. Toda, H. Oogo, K. Horikawa, K. Uesugi, A. Takeuchi, Y. Suzuki, M. Nakazawa, Y. Aoki, M. Kobayashi, The true origin of ductile fracture in aluminum alloys, Metall. Mater. Trans. A 45 (2) (2014) 765–776.
[15] F.A. McClintock, A criterion for ductile fracture by growth of holes, Appl. Mech. (1968) 363–371.
[16] J.R. Rice, D.M. Tracey, On the ductile enlargement of voids in triaxial stress fields, J. Mech. Phys. Solids 17 (3) (1969) 201–217.
[17] J.W. Hancock, A.C. Mackenzie, On the mechanisms of ductile failure in high-strength steels subjected to multi-axial stress-states, J. Mech. Phys. Solids 24 (2–3) (1976) 147–169.
[18] A. Needleman, V. Tvergaard, An analysis of ductile rupture in notched bars, J. Mech. Phys. Solids 32 (6) (1984) 461–490.
[19] G.R. Johnson, W.H. Cook, Fracture characteristics of three metals subjected to various strains, strain rates, temperatures and pressures, Eng. Fract. Mech. 21 (1) (1985) 31–48.
[20] M.S. Mirza, D.C. Barton, P. Church, The effect of stress triaxiality and strain-rate on the fracture characteristics of ductile metals, J. Mater. Sci. 31 (2) (1996) 453–461.
[21] M. Alves, N. Jones, Influence of hydrostatic stress on failure of axisymmetric notched specimens, J. Mech. Phys. Solids 47 (3) (1999) 643–667.
[22] T. Børvik, O.S. Hopperstad, T. Berstad, M. Langseth, A computational model of viscoplasticity and ductile damage for impact and penetration, Eur. J. Mech. A Solids 20 (5) (2001) 685–712.
[23] E. El-Magd, M. Brodmann, Influence of precipitates on ductile fracture of aluminium alloy AA7075 at high strain rates, Mater. Sci. Eng. A 307 (1–2) (2001) 143–150.
[24] M. Fourmeau, T. Børvik, A. Benallal, O.-G. Lademo, O.S. Hopperstad, On the plastic anisotropy of an aluminium alloy and its influence on constrained multiaxial flow, Int. J. Plast. 27 (12) (2011) 2005–2025.
[25] S. Basu, A.A. Benzerga, On the path-dependence of the fracture locus in ductile materials: Experiments, Int. J. Solids Struct. 71 (2015) 79–90.
[26] Y. Bao, T. Wierzbicki, On fracture locus in the equivalent strain and stress triaxiality space, Int. J. Mech. Sci. 46 (1) (2004) 81–98.
[27] I. Barsoum, J. Faleskog, Rupture mechanisms in combined tension and shear—Experiments, Int. J. Solids Struct. 44 (6) (2007) 1768–1786.
[28] X. Gao, T. Zhang, M. Hayden, C. Roe, Effects of the stress state on plasticity and ductile failure of an aluminum 5083 alloy, Int. J. Plast. 25 (12) (2009) 2366–2382.
[29] M. Dunand, D. Mohr, On the predictive capabilities of the shear modified Gurson and the modified Mohr–Coulomb fracture models over a wide range of stress triaxialities and Lode angles, J. Mech. Phys. Solids 59 (7) (2011) 1374–1394.
[30] G. Gruben, O.S. Hopperstad, T. Børvik, Evaluation of uncoupled ductile fracture criteria for the dual-phase steel Docol 600DL, Int. J. Mech. Sci. 62 (1) (2012) 133–146.
[31] J. Faleskog, I. Barsoum, Tension–torsion fracture experiments—Part I: Experiments and a procedure to evaluate the equivalent plastic strain, Int. J. Solids Struct. 50 (25–26) (2013) 4241–4257.
[32] S.S. Haltom, S. Kyriakides, K. Ravi-Chandar, Ductile failure under combined shear and tension, Int. J. Solids Struct. 50 (10) (2013) 1507–1522.
[33] M. Scales, N. Tardif, S. Kyriakides, Ductile failure of aluminum alloy tubes under combined torsion and tension, Int. J. Solids Struct. 97–98 (2016) 116–128.
[34] B. Erice, C.C. Roth, D. Mohr, Stress-state and strain-rate dependent ductile fracture of dual and complex phase steel, Mech. Mater. 116 (2018) 11–32.
[35] F. Hannard, T. Pardoen, E. Maire, C. Le Bourlot, R. Mokso, A. Simar, Characterization and micromechanical modelling of microstructural heterogeneity effects on ductile fracture of 6xxx aluminium alloys, Acta Mater. 103 (2016) 558–572.
[36] B.H. Frodal, K.O. Pedersen, T. Børvik, O.S. Hopperstad, Influence of pre-compression on the ductility of AA6xxx aluminium alloys, Int. J. Fract. 206 (2) (2017) 131–149.
[37] G.T. Hahn, A.R. Rosenfield, Metallurgical factors affecting fracture toughness of aluminum alloys, Metall. Trans. A 6 (4) (1975) 653–668.
[38] M.S. Remøe, K. Marthinsen, I. Westermann, K. Pedersen, J. Røyset, C. Marioara, The effect of alloying elements on the ductility of Al-Mg-Si alloys, Mater. Sci. Eng. A 693 (2017) 60–72.
[39] I. Westermann, K.O. Pedersen, T. Børvik, O.S. Hopperstad, Work-hardening and ductility of artificially aged AA6060 aluminium alloy, Mech. Mater. 97 (2016) 100–117.
[40] S. Thomesen, Plastic flow and fracture of isotropic and anisotropic 6000-series aluminium alloys: experiments and numerical simulations (Ph.D. thesis), Norwegian University of Science and Technology, Trondheim, Norway, 2019.

[41] M. Fourmeau, T. Børvik, A. Benallal, O.S. Hopperstad, Anisotropic failure modes of high-strength aluminium alloy under various stress states, Int. J. Plast. 48 (2013) 34–53.
[42] P.W. Bridgman, The stress distribution at the neck of a tension specimen, Trans. Am. Soc. Met. 32 (1944) 553–574.
[43] G. Le Roy, J.D. Embury, G. Edwards, M.F. Ashby, A model of ductile fracture based on the nucleation and growth of voids, Acta Metall. 29 (8) (1981) 1509–1522.
[44] O.R. Myhr, Ø. Grong, C. Schäfer, An extended age-hardening model for Al-Mg-Si alloys incorporating the room-temperature storage and cold deformation process stages, Metall. Mater. Trans. A 46 (12) (2015) 6018–6039.
[45] M. Khadyko, O.R. Myhr, S. Dumoulin, O.S. Hopperstad, A microstructure-based yield stress and work-hardening model for textured 6xxx aluminium alloys, Phil. Mag. 96 (11) (2016) 1047–1072.
[46] D.J. Lloyd, The scaling of the tensile ductile fracture strain with yield strength in Al alloys, Scr. Mater. 48 (4) (2003) 341–344.
[47] G. Liu, S. Scudino, R. Li, U. Kühn, J. Sun, J. Eckert, Coupling effect of primary voids and secondary voids on the ductile fracture of heat-treatable aluminum alloys, Mech. Mater. 43 (10) (2011) 556–566.
[48] B.H. Frodal, L.E.B. Dæhli, T. Børvik, O.S. Hopperstad, Modelling and simulation of ductile failure in textured aluminium alloys subjected to compression-tension loading, Int. J. Plast. 118 (2019) 36–69.